Supplementary Information

Supplementary Note 1: Quantum Confinement in 2D_EA and 2D_PEA Perovskites

The strength of quantum confinement is mainly determined by the width of inorganic layer (as long as the band gap of organic insulating layer is much larger than that of inorganic semiconductor layer), and slightly related to the width of organic insulating layer. In 2D_EA and 2D_PEA perovskites, their inorganic layer width is the same, while the organic layer width in 2D_EA perovskites is about half of that in 2D_PEA perovskites (Figure 1 a, b), indicating the quantum confinement in 2D_EA is a little smaller than that in 2D_PEA perovskites. The DFT results show the band gap of 2D_EA (2.12 eV) is a little smaller than that of 2D_PEA (2.28 eV) as shown in Supplementary Figure 3. The slightly smaller band gap of 2D_EA perovskites demonstrate that the quantum confinement is a little weaker than that of 2D_PEA perovskites.

The quantum confinement also affects the carrier mobility[1]. According to "sixth-power law", the carrier mobility $\mu \propto 1/d^6$ [2]. The width of quantum wells in 2D_EA and 2D_PEA perovskites are the same, so the effect of quantum confinement on carrier mobility is the same as well. As a result, the improved carrier mobility we measured in 2D_EA perovskites comes from the dielectric confinement reduction.

Supplementary Note 2: Numerical Simulation of Exciton Binding Energy by Image Charge Model

We consider a quantum well system: the semiconductor well (dielectric constant ε_1 and width l) is confined by organic barrier layers (dielectric constant ε_2) whose band gap is much larger. When an electron in the valence band of inorganic layer is excited to the conduction band by a photon, an exciton is created, which is confined in the inorganic layer because their movement through the organic barrier is forbidden. In the case of dielectric constant mismatch at the interface of inorganic layer and organic layer, boundary charges are induced, leading to screening effect to the Coulomb potential between electron and hole in the exciton. We use image charge model[3] to calculate the binding energy.

We assume the position of electron and hole are $(\mathbf{r}_1, z_1)$ and $(\mathbf{r}_2, z_2)$ respectively, where $\mathbf{r}_1$ and $\mathbf{r}_2$ mean the polar coordinates in *x*-*y* plane. The Coulomb potential between the electron at and hole at can be written as:

$$V_{eh} = -\frac{e^2}{4\pi\varepsilon_1\varepsilon_0}\sum_{n=0}^{\infty}\left(\frac{\varepsilon_1-\varepsilon_2}{\varepsilon_1+\varepsilon_2}\right)^n \times\left(\frac{1}{\sqrt{(\mathbf{r}_1-\mathbf{r}_2)^2+[z_1-(-1)^n z_2-nl]^2}} + \frac{1}{\sqrt{(\mathbf{r}_1-\mathbf{r}_2)^2+[z_1-(-1)^n z_2+nl]^2}}\right)$$

Here $\left(\frac{\varepsilon_1-\varepsilon_2}{\varepsilon_1+\varepsilon_2}\right)^n \times e$ is the *n*th image charge. The last term includes two parts, one for the image charge of the above interface and the other one for that of the below interface.

The effective Hamiltonian can be written as:

$$H = -\frac{\hbar^2}{2\mu}\nabla_{\mathbf{r}}^2 - \frac{\hbar^2}{2m_e}\frac{\partial^2}{\partial z_1^2} - \frac{\hbar^2}{2m_h}\frac{\partial^2}{\partial z_2^2} + V_{eh}$$

Here $\vec{r} = \vec{r}_1 - \vec{r}_2$, m_e is the mass of electron, m_h is the mass of hole, μ is the reduced mass of exciton. We neglect the self-energies between electron (hole) and image charges caused by electron (hole) since they don't contribute to the binding energy.

To estimate the binding energy, we use the variational method. We choose trial function

$$|\varphi\rangle = \frac{2}{la}\left(\frac{2}{\pi}\right)^{1/2} \times \cos\left(\frac{\pi z_1}{l}\right) \times \cos\left(\frac{\pi z_2}{l}\right) \times e^{-r/a}$$

In which $r = |\mathbf{r}|$, and a is the variational parameter. Then the exciton binding energy is

$$E_{ex}(a) = \langle\varphi|H|\varphi\rangle_\infty - \langle\varphi|H|\varphi\rangle_a = -\left\langle\varphi\left|-\frac{\hbar^2}{2\mu}\nabla_{\vec{r}}^2 + V_{eh}\right|\varphi\right\rangle$$

We let $dE_{ex}(a)/da = 0$ to get the 2D Bohr radius a and thus get the binding energy $E_{ex}(a)$.

To investigate the effect of dielectric constant of organic groups on the exciton binding energy and Bohr radius, we assume the width of inorganic well is 0.6 nm, the effective reduced mass of exciton is $0.1 \times m_0$ where m_0 is the mass of electron. We fix the dielectric constant of inorganic layer ε_1 at 6.1, and vary the dielectric constant of organic layer ε_2. To the cases of EA and PEA, we use dielectric constant of 37.7 and 3.3 respectively.

Supplementary Note 3: Band Structure and Effective Mass

The density functional theory (DFT) calculations were performed using PWSCF code implemented in Quantum ESPRESSO package. The generalized gradient approximation (GGA) together with Perdew-Burke-Ernzerhof (PBE) method was used to optimize the crystal structures for both 2D_EA and 2D_PEA hybrid perovskites. The ultrasoft scalar-relativistic and relativistic pseudopotentials (without and with spin-orbit coupling) were used to describe the electron-ion interactions by explicitly treating electrons for H ($1s^1$), C, N, and O ($2s^2$, $2p^2$), I ($5s^2$, $5p^2$), and Pb ($5d^{10}$, $6s^2$, $6p^2$). Single-particle wave functions (charges) were expanded on a plane-wave basis set up to a kinetic energy cutoff of 50 Ry (300 Ry), here Ry is Rydberg constant, for both crystal structures. Monkhorst−Pack-type K-meshes of 6 × 6 × 6 for $(EA)_2PbI_4$ and 6 × 6 × 4 for $(PEA)_2PbI_4$ were used. Each crystal structure was optimized until the forces on each single atom were smaller than 0.01 eV/Å. From the calculated band structure diagram, the band gaps of 2D_EA and 2D_PEA perovskites are 2.12eV and 2.28eV, which are close to PL data. The effective masses along the Pb-I framework in those two 2D perovskites are shown in Supplementary Table 1.

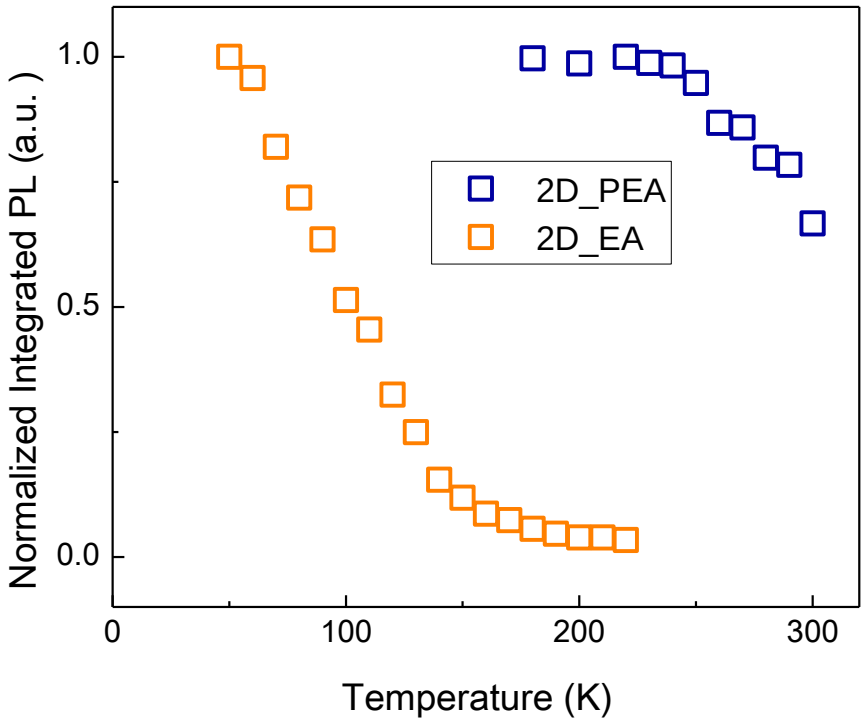

Supplementary Figure 1 | Temperature-dependent integrated PL of 2D_EA and 2D_PEA perovskites.

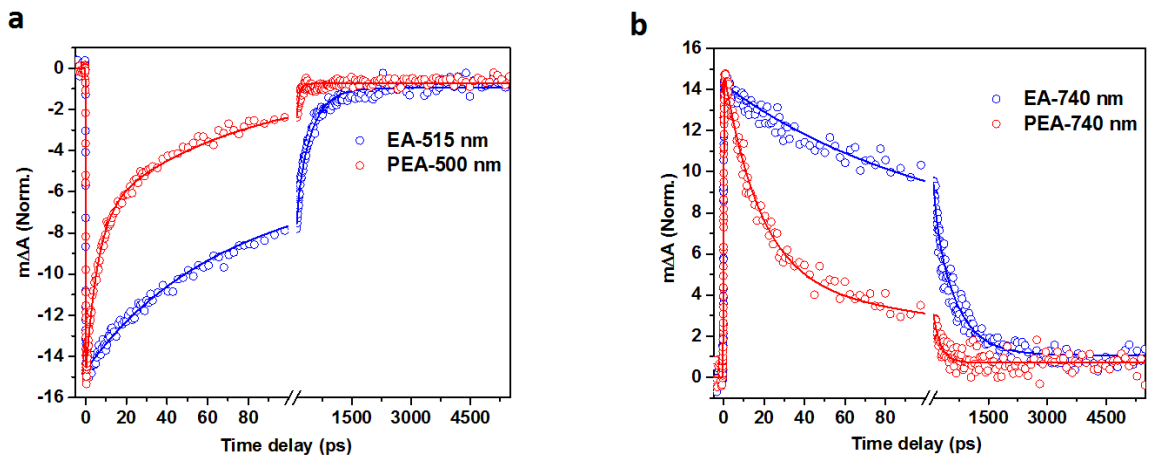

Supplementary Figure 2 | Normalized ground state bleach recovery kinetics probed at bleach maxima **a:** and excited state decay probed at 740 nm **b:** following 330 nm optical excitation of 2D perovskite.

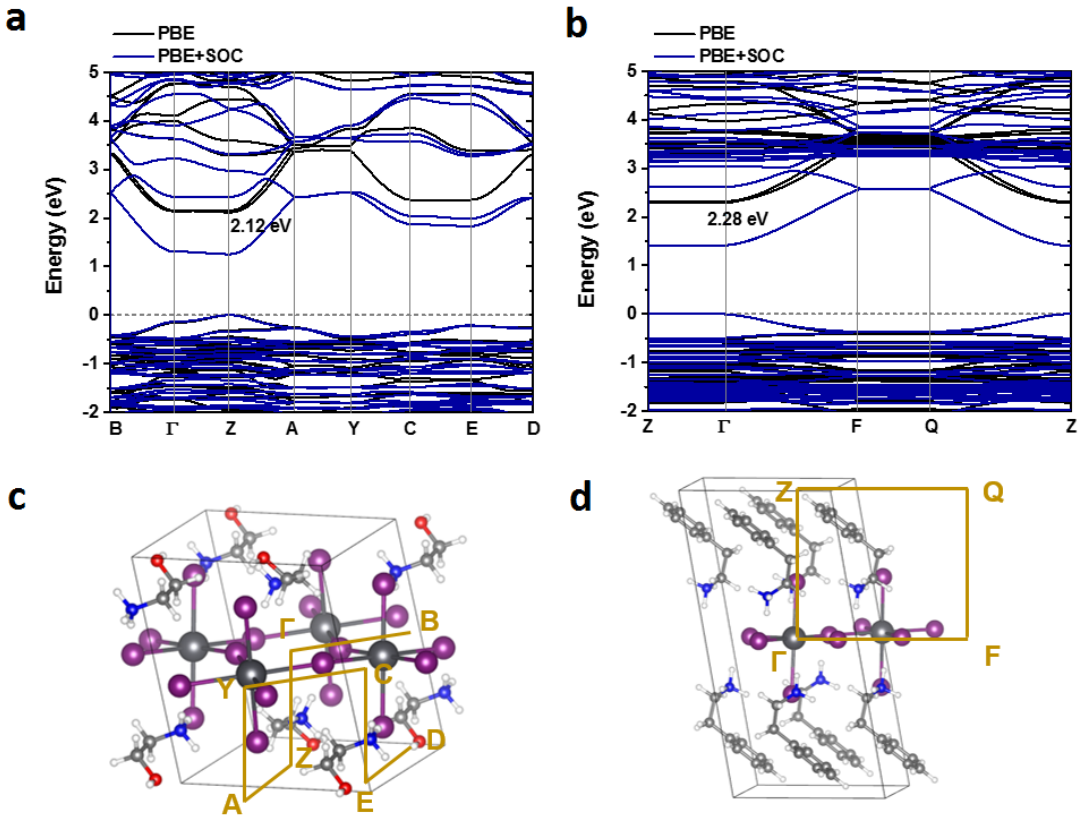

Supplementary Figure 3 | Electronic properties and band structure. Simulated band diagram and corresponded crystallographic structure of **a,** 2D_EA **b,** 2D_PEA perovskites. The high symmetry points in the Brillouin zone **c,** in 2D_EA and **d,** 2D_PEA perovskite respectively.

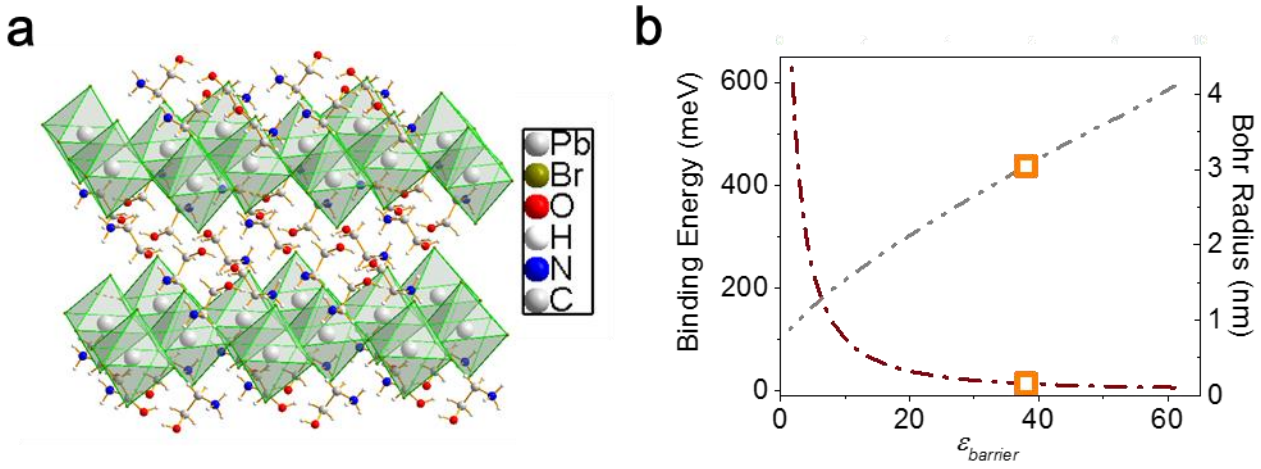

Supplementary Figure 4 | Crystallographic structure and exciton binding energy. Lattice structure of **a,** EA_2PbBr_4 **b**, Exciton binding energy and Bohr radius as a function of organic-group dielectric constant in EA_2PbBr_4 perovskite according to the Image Charge Model.

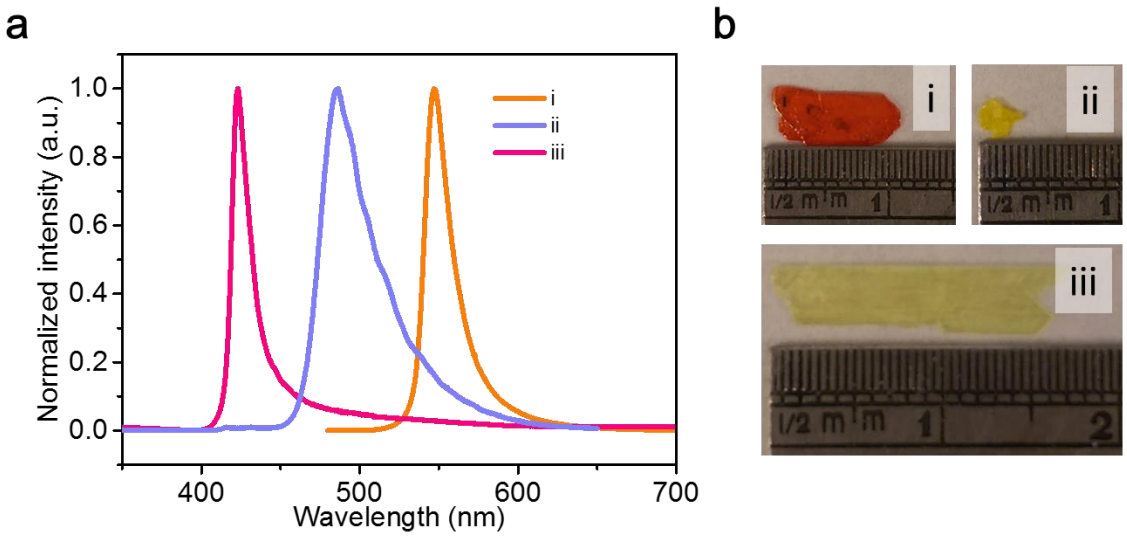

Supplementary Figure 5 | 2D perovskites with different Halogen ions. a, photoluminescence of (i) $(HOC_2H_4NH_3)_2PbI_4$, (ii) $(HOC_2H_4NH_3)_2PbI_2Br_2$, and (iii) $(HOC_2H_4NH_3)_2PbBr_4$. **b,** photo image of $(HOC_2H_4NH_3)_2PbI_4$ (i), $(HOC_2H_4NH_3)_2PbI_2Br_2$ (ii), $(HOC_2H_4NH_3)_2PbBr_4$ (iii).

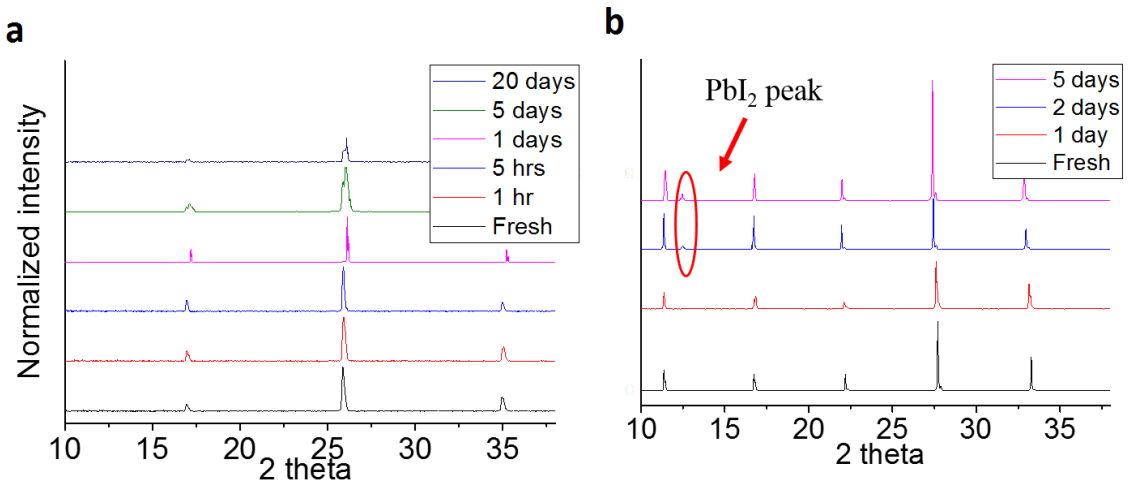

Supplementary Figure 6 | Time dependent powder XRD. **a:** 2D_EA perovskite; **b:** 2D_PEA perovskite.

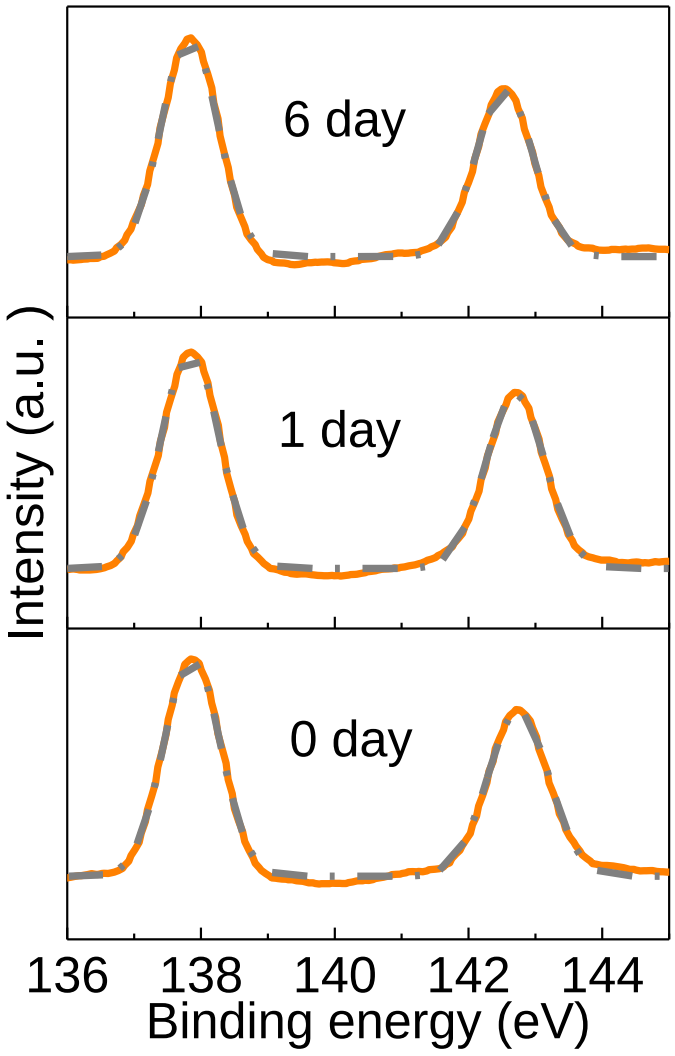

Supplementary Figure 7 | Humidity stability. XPS of Pb 4f5/2 and 4f7/2 region of 2D_EA single crystals and the fitting curve (grey dash).

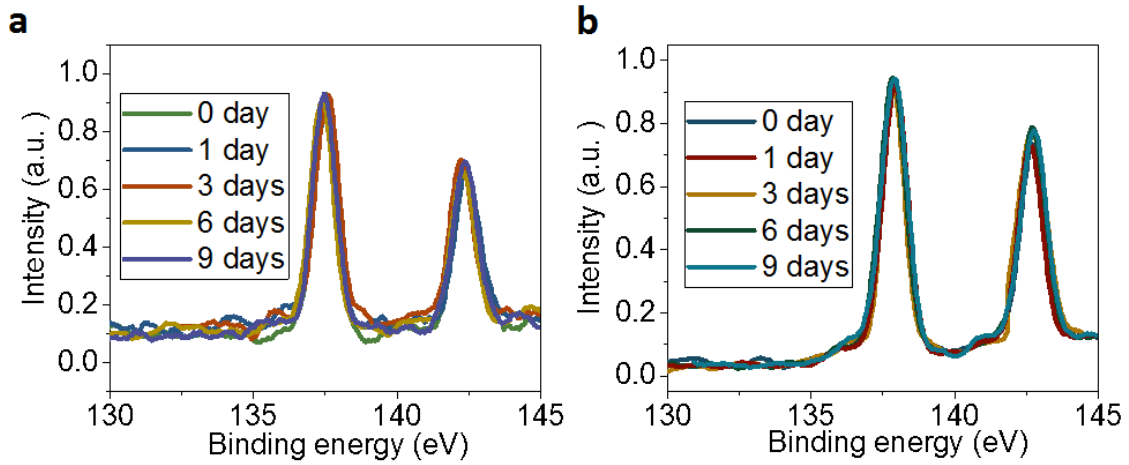

Supplementary Figure 8 | Humidity stability. XPS measurements under **a,** 360 eV and **b,** 600 eV injective X-ray of Pb $4f_{5/2}$ region of 2D_EA single crystals with different exposed days in 60% RH, 20°C.

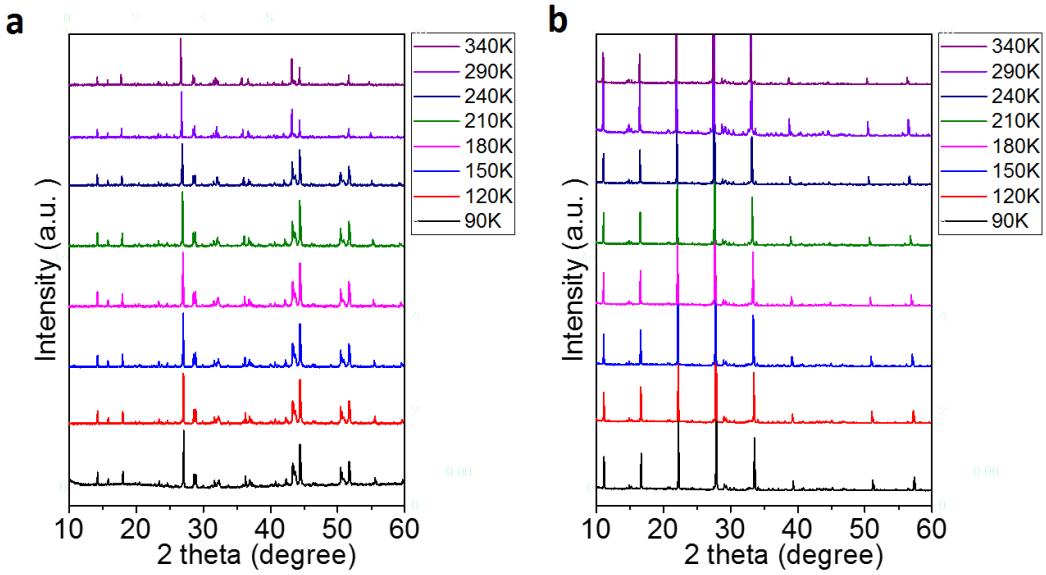

Supplementary Figure 9 | Temperature-dependent powder x-ray diffraction of a, 2D_EA and **b,** 2D_PEA perovskite powder which are grounded from 2D_EA and 2D_PEA perovskite single crystals, respectively.

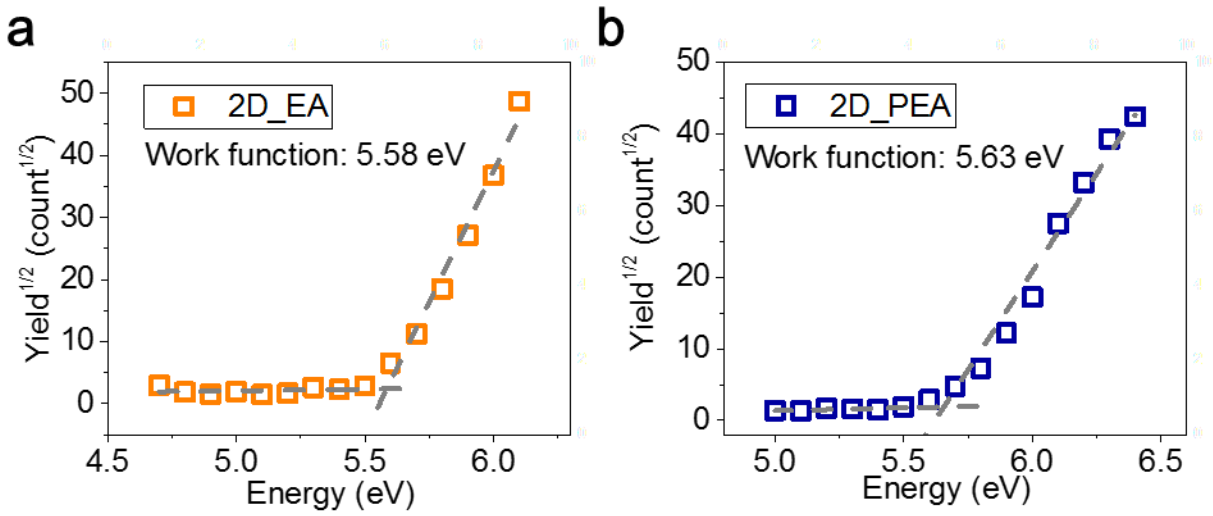

Supplementary Figure 10 | Photo-Electron Spectroscopy in Air of a, 2D_EA and **b,** 2D_PEA perovskite single crystals.

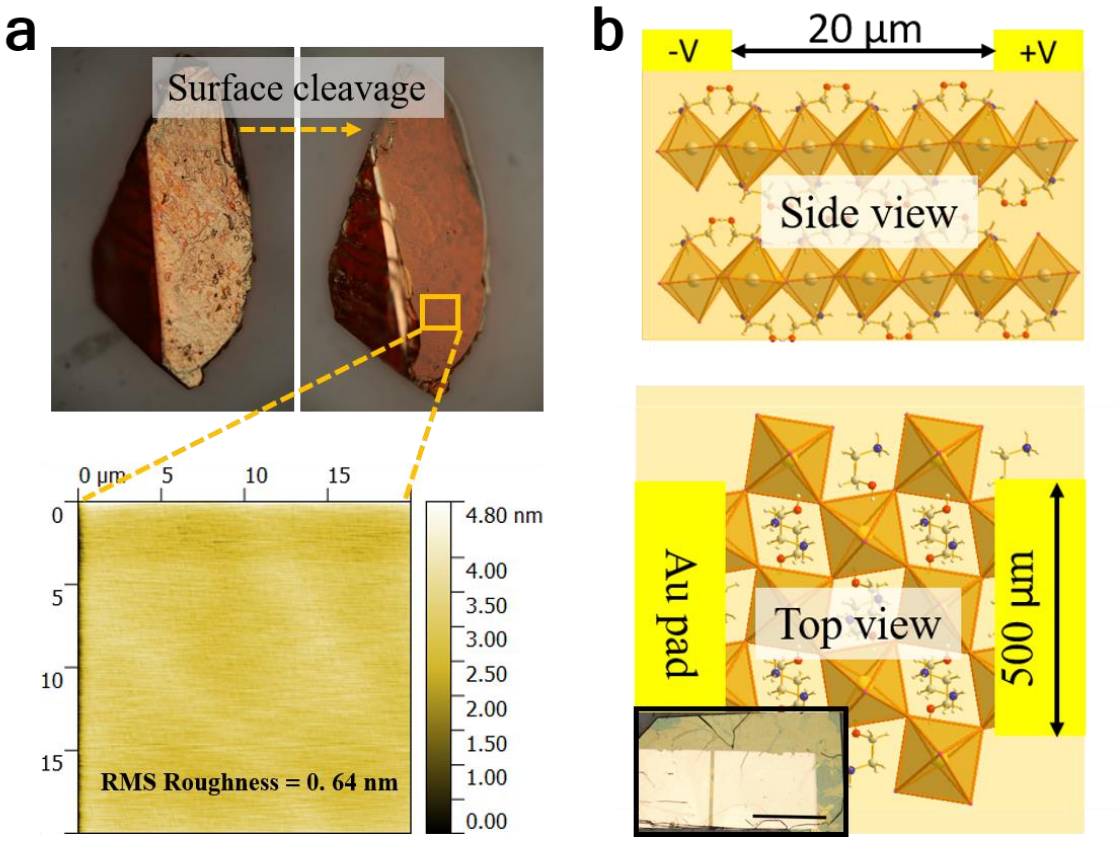

Supplementary Figure 11 | Surface cleavage and 2D perovskite MSM junction. a, optical and atomic force microscopy image of 2D_EA crystal. **b,** Illustration of 2D_EA MSM junction. Inset of 2b down shows the MSM junction with a 200 um scale bar.

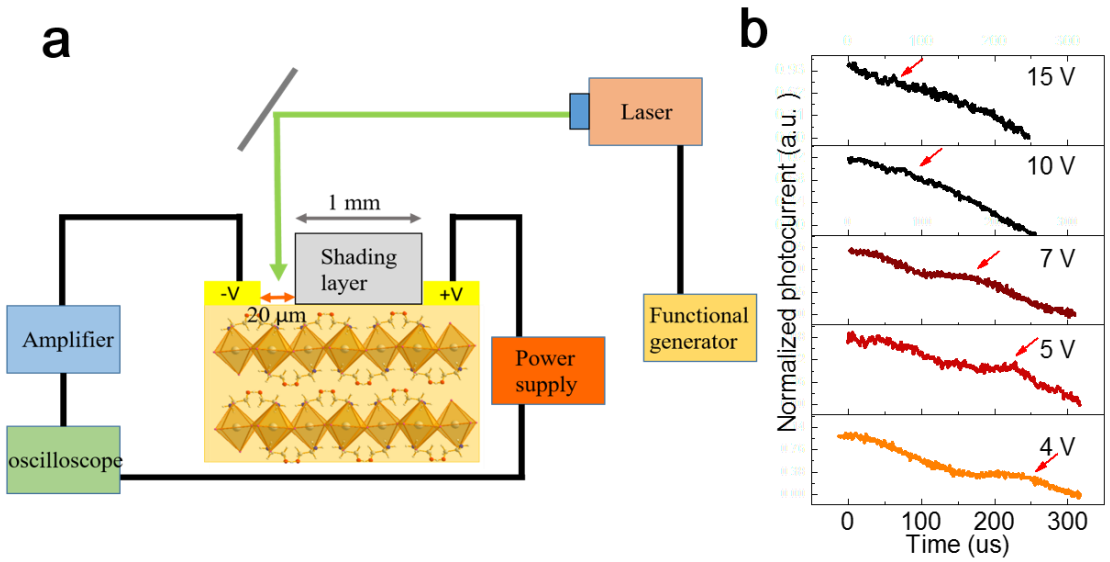

Supplementary Figure 12 | Time of Flight (TOF) setup and data. a, Setup of TOF, The Power supply is using Keithley 4200SCS, the oscilloscope is using Agilent DSO 5034A, the amplifier is using SRS SR570, the 520 nm laser is using, the pulse function generator is using Agilent 81150A. **b**, TOF photocurrent signal for bias voltage from 4 V to 15 V. The red arrays indicate the transit time of carrier transport.

Supplementary Table 1. Calculated effective mass (m^*, × m_0) along the Pb-I framework of $(EA)_2PbI_4$ and $(PEA)_2PbI_4$ hybrid perovskites without and with Spin-orbit coupling effects (in bracket).

effective mass (×m_0)	**$(EA)_2PbI_4$**	**$(PEA)_2PbI_4$**
Electron	Z-A: 0.232 (0.234)	Γ-F: 0.266 (0.153)
Hole	Z-A: 0.759 (0.905)	Γ-F: 0.255 (0.220)

1 Milot, R. L. *et al.* Charge-carrier dynamics in 2D hybrid metal–halide perovskites. *Nano letters* **16**, 7001-7007 (2016).
2 Ma, N. & Jena, D. Charge scattering and mobility in atomically thin semiconductors. *Physical Review X* **4**, 011043 (2014).
3 Hanamura, E., Nagaosa, N., Kumagai, M. & Takagahara, T. Quantum wells with enhanced exciton effects and optical non-linearity. *Materials Science and Engineering: B* **1**, 255-258 (1988).